Solar irradiance forecast using aerosols measurements: A data driven approach

Abdullah Alfadda*, Saifur Rahman, Manisa Pipattanasomporn

Virginia Tech – Advanced Research Institute, Arlington, VA 22203, USA

ARTICLE INFO

ABSTRACT

The use of renewable energy resources has grown several fold in the last two decades. One of the main challenges is the uncertainty in their output power due to fluctuating meteorological conditions like sunshine intensity, cloud cover and humidity. In desert areas, another parameter that has a significant impact on solar irradiance is dust, which has been neglected in many studies. In this work, an hour-ahead solar irradiance forecasting model is proposed, this model utilizes both Aerosol Optical Depth (AOD) and the Angstrom Exponent data observed from a ground station at the previous hour. The proposed model was tested under different widely used data driven forecasting models, including Multilayer Perceptron (MLP), Support Vector Regression (SVR), k-nearest neighbors (kNN) and decision tree regression. Applying the MLP model using data from Saudi Arabia shows a root mean square average error of under 4% and forecast skill of over 42% for one-hour ahead forecast. The proposed forecasting model demonstrates a superior accuracy compared to other models when tested and verified under different feature selection schemes. The MLP model is especially applicable for desert areas under clear sky conditions, where dust storms are frequent and AOD in the air is high (> 0.4).

1. Introduction

Renewable energy resources represent 24% of the total electrical energy generated worldwide as of 2016 (IEA, 2017), and the solar share is only 1.2%. Many countries around the world have plans to invest in large-scale renewable energy projects. However, the main issue with these resources is the uncertainty in their output power, which can result in an overall power grid instability. With respect to solar power, this can be caused by the fluctuation in many meteorological variables, such as cloud cover, temperature and wind speed. Thus, solar irradiance forecasting is of great importance for grid operators, allowing them to ensure the stability of the power grid, optimally set demand response schedules, economic dispatch and optimize power plant operations.

Saudi Arabia is one of the countries that have ambitious plans to decrease their dependence on oil and natural gas for energy production. In 2016 Saudi Arabia revealed that the country plans to produce 9.5 GW of energy from renewable resources by 2023 (Asif, 2016), with an initial target of 3.45 GW by 2020. The expected total electricity generation in the country will be around 95 GW by 2023 (Abdel Gelil et al., 2017). One main issue when installing solar Photovoltaics (PV) in desert areas like Saudi Arabia is the frequent occurrence of dust storms (Hassan et al., 2017). The dusty weather results in less accurate solar irradiance forecasts. Moreover, the overall PV module efficiency

decreases due to dust accumulation over the module's surfaces. In Notaro et al. (2013) they provided a detailed dust assessment all over the country with trajectory analysis.

Solar irradiance is directly dependent on multiple weather factors, mainly cloud cover, humidity and visibility, besides other parameters, such as ground albedo. Thus, better forecasts of these weather factors would result in an improved solar irradiance model. However, in some areas that have low cloud cover, the solar forecasts would be more affected by the remaining factors. Moreover, areas like Arabian Peninsula and North Africa are exposed to frequent dust storms and high aerosols index all over the year. Thus, developing a solar irradiance forecasting model that incorporates the dust phenomena is of a great importance for such areas.

Some work has been carried out to investigate the relationship between the PV module efficiency and dust accumulation over PV panels (Sarver et al., 2013; Sulaiman et al., 2014). In Jiang et al. (2016), authors studied the optimum cleaning frequency for the PV module to improve module efficiency. In Alqatari et al. (2015) authors have compared the cost and performance of different PV cleaning techniques.

The other main concern due to the presence of dust in the air is the increased uncertainty in solar radiation forecast. Moreover, the forecasted Aerosol Optical Depth (AOD) values are not fully correlated with
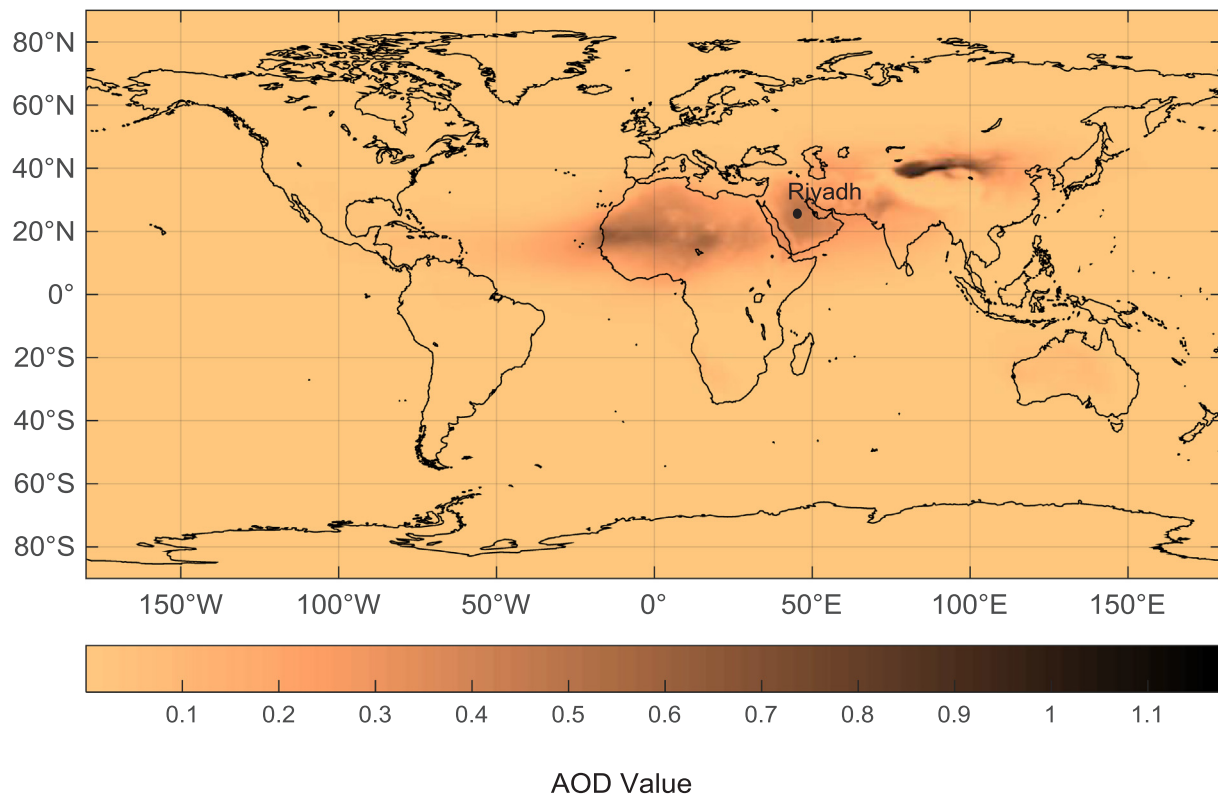

Fig. 1. Annual average AOD at 550 nm over the world for the year 2015 using CAMS dataset.

the ground-based AOD measurement. In Cesnulyte et al. (2014) authors compared AErosol RObotic NETwork (AERONET) data with European Center for Medium-Range Weather Forecasts (ECMWF) readings across multiple sites around the world, the average correlation coefficient found to be 0.77 for dust areas. Thus, uncertainty in forecasted AOD values would lead to a lower solar forecasting accuracy, especially in desert areas, where cloud-free environments are dominant and dust particles have frequent presence in the air.

Machine learning techniques have been widely used in solar irradiance forecasting. Artificial Neural Networks (ANNs) are the most widely used techniques for solar forecasting (Antonanzas et al., 2016), which have been applied to both short-term (Gutierrez-Corea et al., 2016) and long-term forecasting (Azadeh et al., 2009). ANN with more than one hidden layer is usually referred to as Multilayer Perceptron (MLP). k-Nearest Neighbors (kNN) has also been widely used in the literature, it has been applied to predict intra hour irradiances (Pedro and Coimbra, 2015a), and to generate probabilistic forecasts (Chu and Coimbra, 2017). Other machine learning methods have also been applied to solar forecasting, such as Support Vector Regression (SVR) (Belaid and Mellit, 2016), random forests (Ibrahim and Khatib, 2017) and Lasso (Yang et al., 2015). Machine learning techniques have also been used in solar forecasting with AOD as input, in Eissa et al. (2013) they used six thermal channels from SEVERI satellite images to predict the aerosols at 550 nm, then fed this prediction to ANN model to improve the Global Horizontal Irradiance (GHI), Direct Normal Irradiance (DNI) and Diffuse Horizontal Irradiance (DHI) forecasts.

Newer techniques such as deep learning has also been implemented in a number of time series forecasting models (Li et al., 2017; Qiu et al., 2014; Ryu et al., 2016), it has shown a superior accuracy compared to other machine learning methods. It was implemented to estimate the building energy consumption (Mocanu et al., 2016), predict the wind speed (Hu et al., 2016) and forecast the solar irradiance (Alzahrani et al., 2017). Convolutional version of deep learning has been implemented to predict the Photovoltaic output power (Wang et al., 2017) using both deterministic and probabilistic approaches. In Gensler et al.

(2017) they implemented Long Short Term Memory (LSTM) version of deep learning to forecast the PV output power for the next day. Convolutional LSTM version was used to predict the short-term precipitation based on spatiotemporal data sequence (Shi et al., 2015). Spatiotemporal data were also studied using other methods such as Kriging (Jamaly and Kleissl, 2017) and applied to solar irradiance forecasting.

Solar forecasting time horizon can be categorized into short-term, medium-term and long-term forecasting. In the short-term forecasting the predicted solar irradiance value falls within the next few hours, multiple short-term models have been developed in the literature (Ghayekhloo et al., 2015; Pedro and Coimbra, 2015b; Rana et al., 2016). The medium-term forecasts generate predictions that cover the span of the next few days (Gulin et al., 2017; Pierro et al., 2016). Lastly, long-term forecasts predict the solar irradiance for the next few months to years (Ruiz-Arias et al., 2016a, 2016b).

The ground-based AOD measurement and angstrom exponent never been used altogether in the literature to construct an hour-ahead solar irradiance forecasting model. In this work, a data driven forecasting model under clear sky conditions with a large aerosol presence is proposed, utilizing both the ground-based AOD measurements observed at the last hour alongside the angstrom exponent and other weather parameters. All of the parameters are fed into the data driven solar forecasting model, which results in a more accurate (GHI/DNI/DHI) forecast for the next hour. The use of ground-based AOD measurements would result in a better AOD forecast accuracy for the next hour, and hence better (GHI/DNI/DHI) forecasting. The model was trained using hourly data collected from three different resources, i.e., King Abdullah City for Atomic and Renewable Energy (KACARE), Copernicus Atmosphere Monitoring Service (CAMS) and AERONET over the period of three years 2013–2015. The test site is in Riyadh, Saudi Arabia, chosen because it is frequently exposed to different degrees of dust storms over the year, ranging from mild to severe storms (Nabavi et al., 2016). Annual average AOD at 550 nm over the world for the year 2015 is shown in Fig. 1, as can been seen from Fig. 1 the test location reside in area where the average AOD is high. In Fig. 2 the annual average GHI over Saudi Arabia is shown.
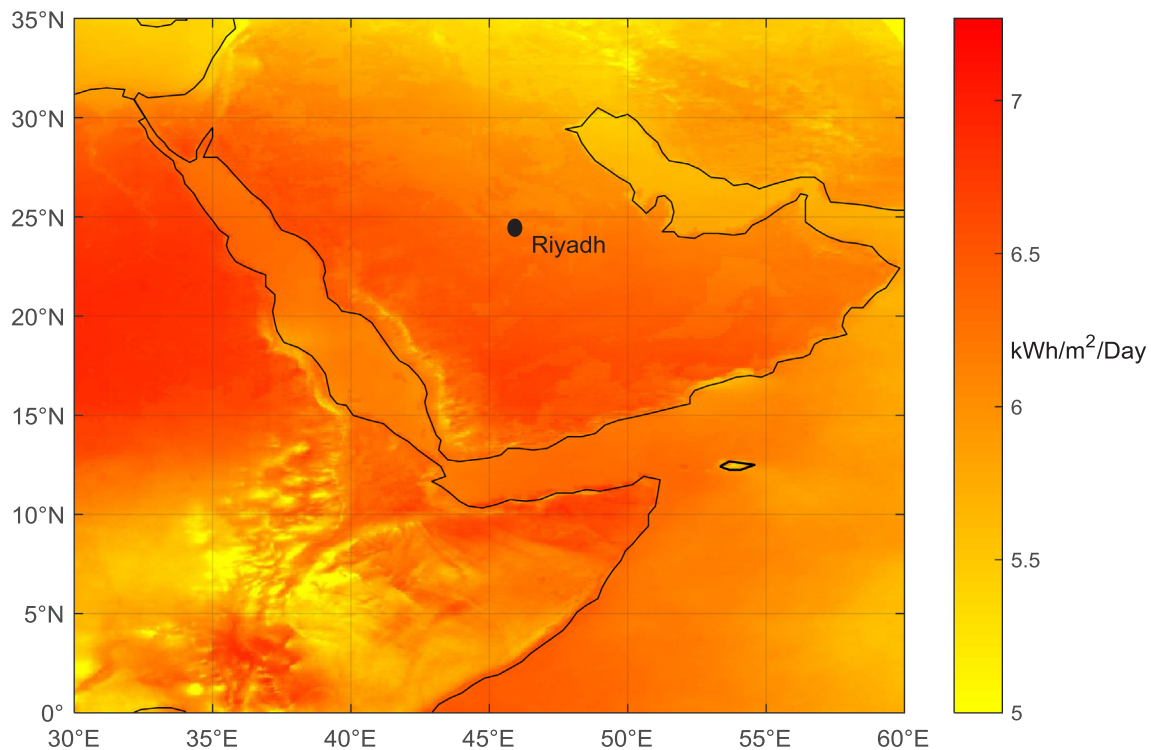
Fig. 2. Annual GHI over Saudi Arabia for the year 2013 based on Meteosat data.

2. Solar irradiance forecasting methods

In order to design the proposed solar forecasting system, machine learning/data driven approaches were used. Different machine learning methods, namely Multilayer Perceptron (MLP), SVR, kNN and decision tree were implemented. Discussion on each method implemented is provided below. The inputs for these models are listed in Table 1. For each solar irradiance variable (i.e., GHI, DNI and DHI), a forecasting model was generated using these four methods. Each forecasting method was tested under different feature selection schemes as shown in Table 2.

The basic structure of the forecasting model is shown in Fig. 3, where we use ground observed values from the previous hour and the next hour forecasts provided by CAMS. Since the site under study is in a desert area, hence it is dry and has low relative humidity over the tested period (on average 16%). Therefore, this study selectively excludes humidity from the set of predictors.

Table 1
Input variables to the forecasting models.

Input variable	Input variable explanation
x_i^1	Ground measured GHI at last hour
x_i^2	Ground measured DNI at last hour
x_i^3	Ground measured DHI at last hour
x_i^4	Hour of the Day
x_i^5	Month of the Year
x_i^6	Solar Zenith Angle
x_i^7	Wind Speed
x_i^8	Wind Direction
x_i^9	CAMS AOD at 550 nm
x_i^{10}	AERONET AOD at 550 nm observed at last hour
x_i^{11}	Angstrom Exponent α

Table 2
GHI/DNI/DHI forecasting model feature selection schemes.

Variable	Feature selection scheme	Input variables
GHI	1	$x_i^1, x_i^4, \cdots, x_i^7$
	2	$x_i^1, x_i^4, \cdots, x_i^9$
	3	$x_i^1, x_i^4, \cdots, x_i^8, x_i^{10}, x_i^{11}$
DNI	1	$x_i^2, x_i^4, \cdots, x_i^7$
	2	$x_i^2, x_i^4, \cdots, x_i^9$
	3	$x_i^2, x_i^4, \cdots, x_i^8, x_i^{10}, x_i^{11}$
DHI	1	$x_i^3, x_i^4, \cdots, x_i^7$
	2	$x_i^3, x_i^4, \cdots, x_i^9$
	3	$x_i^3, x_i^4, \cdots, x_i^8, x_i^{10}, x_i^{11}$

2.1. Multilayer perceptron

The basic component of any MLP network is a neuron. A single neuron output is calculated based on the summation of the incoming neurons values, originating from the previous layers, then multiplied by the weights on these connections and added to a bias term, finally applied to an activation function, as shown in Eq. (1). The structure of a single neuron is shown in Fig. 4.

$$\varphi = f\left(b + \sum_{i=1}^{n} w_i a_i\right) \tag{1}$$

where b is the bias term; w_i is the weight on each connection; a_i is the value of each incoming connection; n is the total number of incoming connections for the neuron; f is the activation function; and φ is the output value. The choice of the activation function depends on the problem on hand. For time series predictions, Rectified Linear Unit (ReLU) has proved to have the best accuracy performance compared to all other activation functions. Eq. (2) shows the updated neuron output φ after applying the ReLU activation function.
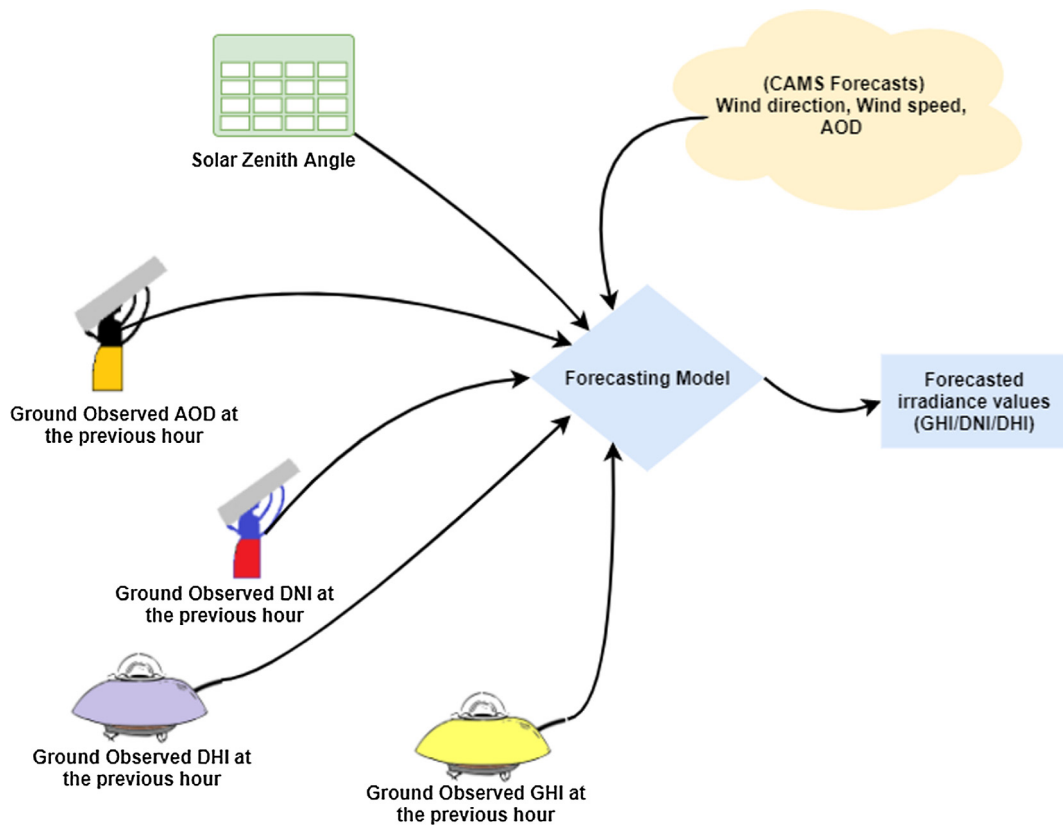
Fig. 3. Basic structure of the forecasting model.

$$\varphi = \max\left(0,\, b + \sum_{i=1}^{n} w_i a_i\right) \qquad (2)$$

Neurons are only the building blocks of the MLP model. The basic structure of the proposed model is illustrated in Fig. 5.

The first layer is the input layer (in green), which is the input data (i.e., training data) entry points to the network that will construct model parameters. Subsequent layers (in grey) are the hidden layers. The MLP network could have as many hidden layers as needed, the number of hidden layers and the structure of the network is highly dependent on the application. This work involved two hidden layers as any additional hidden layers do not contribute to the model's overall accuracy.

The input data points of the proposed model are defined as $X_i = [x_i^1, x_i^2, \cdots, x_i^l]$, and their labels are y_i, where $i \in \{1, 2, \cdots n\}$, n is the total number of training data points and l is the total number features

for the input data point. The output of each data point X_i is denoted as $h\langle X_i, W\rangle$, where W is the set of weights on the connections between the neurons across all of the network.

After the construction of the network, the goal now is to find the optimum set of weights W, such that the error between the actual and the predicted labels values is minimized. In order to achieve this, the squared error loss function (Eq. (3)) is added at the output neuron (denoted in red as shown in Fig. 5), at which the performance of the proposed MLP model is being optimized, by comparing the ground truth labels with the predicted values, during the training phase.

$$L = \frac{1}{2}(h\langle X_i, W\rangle - y_i)^2 \qquad (3)$$

where $h\langle X, W\rangle$ is the predicted value; y_i is the actual value; and L is the total loss. Now, in order to find the optimum W values, the gradient of the loss function L is computed with respect to each weight on the
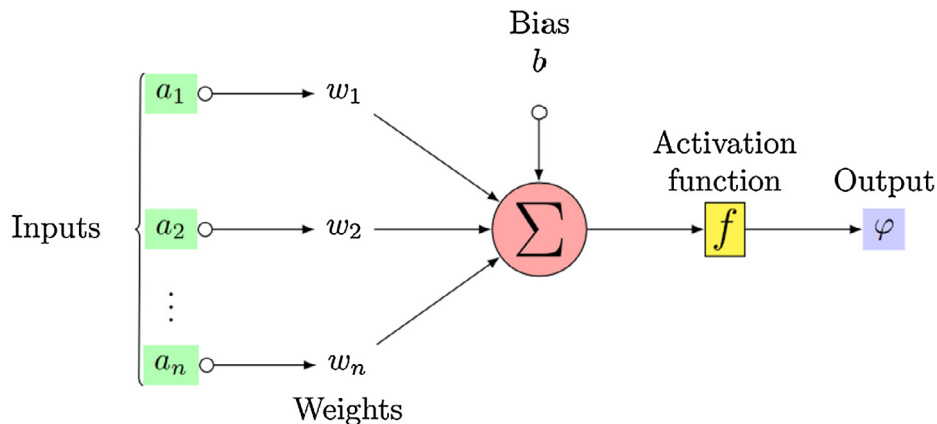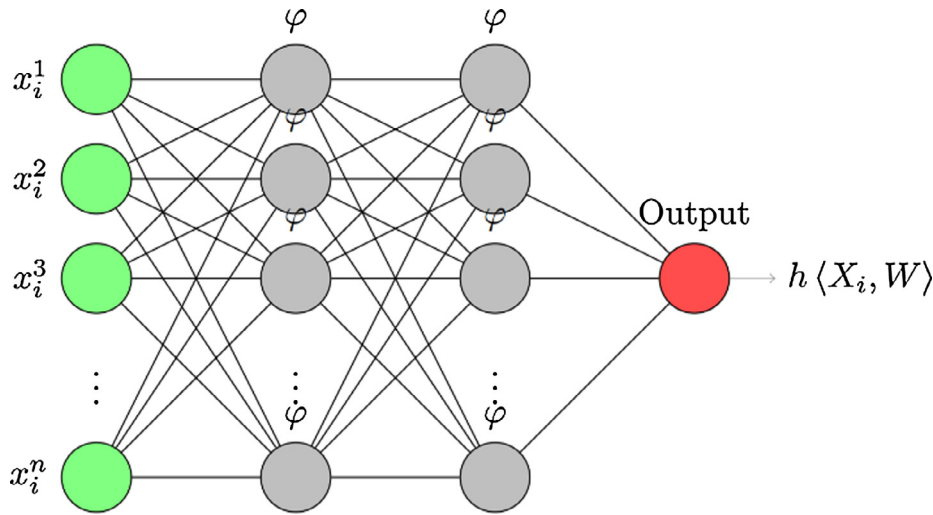

Fig. 4. Neuron structure.

Fig. 5. MLP network structure.

network $w_{j→k}$, where, j and k denote the neuron index; and $w_{j→k}$ denotes the connection between neuron j to neuron k. So, the gradient can be expressed as shown in Eq. (4):

$$\frac{\partial}{\partial w_{i→k}}L(w) = \frac{\partial}{\partial w_{i→k}}\sum_i \frac{1}{2}(h\langle X_i, W\rangle - y_i)^2,$$
$$= \sum_i (h\langle X_i, W\rangle - y_i)\frac{\partial}{\partial w_{i→k}}h\langle X_i, W\rangle. \tag{4}$$

Finally, the gradient for each weight in the network is to be determined, until the optimum value for each weight is reached, i.e., the overall loss is minimized. This would be computationally expensive if classical optimization techniques, e.g., gradient decent, are used. Thus, the Adam solver (Kingma and Ba, 2015) was selected for solving this problem, which proved to perform well on large datasets.

The structure of the implemented MLP network has seven neurons at the first hidden layer and five neurons at the second hidden layer. The number of these neurons at these different layers was selected by adding more neurons and keep tracking the Root Mean Square Error (RMSE) performance, until the error is minimized over the training data. Adding more neurons to the first or second hidden layers does not improve the model's overall accuracy.

2.2. Support Vector Regression

Support Vector Regression (SVR) is a supervised machine learning algorithm. It is extension of Support Vector Machines (SVM) to regression problems. It solves the following optimization problem:

$$\min_{q,\beta,\zeta,\zeta^*} \frac{1}{2}q^t q + C\sum_{i=1}^n (\zeta_i + \zeta_i^*),$$
$$s.\,t.$$
$$y_i - q^t\phi(X_i) - \beta \leqslant \varepsilon + \zeta_i,$$
$$q^t\phi(X_i) - y_i + \beta \leqslant \varepsilon + \zeta_i^*,$$
$$\zeta_i, \zeta_i^* \geqslant 0, i = 1, ..., n, \tag{5}$$

where q is the weight vector; β is the bias term; ξ_i, ξ_i^* are the slack variables; C is a tradeoff variable for the flatness of the curve; and ε is the tolerance variable; $\phi(X_i)$ is the higher dimensional training vector resulted from X_i. After solving the problem for q and β, the test point label $\hat{y}_i$ can be predicted as follows:

$$\hat{y}_i = \langle q, \phi(X_i)\rangle + \beta, \tag{6}$$

where $\langle ., ..\rangle$ is the dot product of q and $\phi(X_i)$. Now, solving for the dual problem of Eq. (5) and the introduction of the Lagrange multipliers, the final solution will be as follows:

$$\hat{y}_j = \sum_{i=1}^n (\delta_i - \delta_i^*)K(X_i, X_j) + \beta, \tag{7}$$

where δ_i, δ_i^* are the Lagrange multipliers and $K(X_i, X_j)$ is the kernel function used to find the dot product between two ϕ without transforming them into the higher dimensional space. Thus, the computational complexity would be lowered significantly, this is commonly known as the kernel trick. SVR error performance could be improved by the use of kernels as well. There are four known kernels used in the literature, linear, Radial Basis Function (RBF), polynomial and sigmoid kernels. The RBF kernel has proved to work well on regression problems in the literature, due to its computational efficiency (Olatomiwa et al., 2015). In this work, RBF was used as Kernel, the mathematical formulation for the kernel is as follows:

$$K(X_i, X_j) = e^{\frac{-\|X_i - X_j\|^2}{2\sigma^2}}. \tag{8}$$

For SVR, similar steps were followed as the MLP. The C value that minimizes the RMSE over the training data was chosen, the optimum C value in this work was found to be 1000.

2.3. kNN regression

kNN is a widely used clustering algorithm. However, it could also be implemented to solve regression problems. For each test point $\hat{x}$ the distance to all training datapoint x_i is to be determined in the dataset as follows:

$$D_i = \sqrt{\sum_j (x_i^j - \hat{x}^j)^2}. \tag{9}$$

For each test point $\hat{x}$ the distance to all training points x_i is computed, then the k nearest neighbors labels values y_i are averaged to predict the $\hat{x}$ label value $\hat{y}$. In this work, kNN was optimized by changing the number of neighbors and tracking the RMSE values over the training data. The RMSE value was at its minimum when the number of neighbors k is five.

2.4. Decision tree regression

Decision trees is a widely used machine learning algorithm, it can be used for both classification and regression. It is constructed by nodes and leafs, each node has different number of branches which would lead to another nodes or leafs. Each test point will start from the root node, then will follow the branches that are tested to be true for that test point, this procedure will be followed until a leaf is reached, then

-19

the predicted value $\hat{y}_i$ of a test point is assigned a value as the value of the leaf that is has reached. The construction of the tree could be done using different algorithms, one of most widely used algorithm is Iterative Dichotomiser 3 (ID3), however, in this work we have implemented the classification and regression trees (CART) algorithm, since it would also solve the regression problem, and not restricted to the classification problem.

2.5. Model evaluation and error measure

2.5.1. Error measure

The evaluation of the model accuracy is based on the RMSE, a widely used error measure in regression problems. The mathematical formulation of the RMSE is shown in Eq. (10):

$$RMSE = \sqrt{\frac{\sum_{i=1}^{n}(\hat{y}_i - y_i)^2}{n}}, \tag{10}$$

where $\hat{y}_i$ is the predicted value at time i; y_i is the actual (ground truth) value and n is the total number of points in the testing dataset.

The second error metric used in this work is the Mean Absolute Percentage Error (MAPE), it is defined as follows:

$$MAPE(\%) = \frac{100}{n}\sum_{i=1}^{n}\left|\frac{\hat{y}_i - y_i}{y_i}\right|. \tag{11}$$

2.5.2. Smart persistence

Smart persistence is the benchmark model implemented in this work, it is based on the deterministic irradiance variation from time t and time $t + T$, calculated from the clear sky model. The smart persistence mathematical formulation is as follows:

$$\hat{I}_{sp}(t + T) = \frac{I_{cs}(t + T)}{I_{cs}(t)}I(t), \tag{12}$$

where $\hat{I}_{sp}(t + T)$ is the smart persistence irradiance prediction at time $t + T$, $I_{cs}(t + T)$ is the clear sky model at time $t + T$, $I_{cs}(t)$ is the clear sky model at time t, $I(t)$ is the irradiance observed value at time t. The Ineichen and Perez clear sky model (Ineichen and Perez, 2002; Perez et al., 2002) was used in this work.

2.5.3. Forecast skill

The performance of the forecasting models need to be normalized by a benchmark. The forecast skill proposed in Coimbra et al. (2013), is a way to normalize and compare the accuracy of the model against the benchmark model. The mathematical formulation of the forecast skill is as follows:

$$FS = 1 - \frac{RMSE_{model}}{RMSE_{sp}}, \tag{13}$$

where FS is the forecast skill value, $RMSE_{model}$ is the RMSE value resulted from the forecasting model, $RMSE_{sp}$ is the RMSE resulted from the smart persistence model. A forecast skill of 0 indicates that the model performance is similar to the smart persistence model. A higher positive FS value indicates that the model has a better performance compared to the smart persistence model, with a maximum FS value of 1. A negative FS value indicates that the forecasting model performs worse than the smart persistence model.

2.5.4. Data splitting

In this work, the available dataset was divided into training and testing subsets. The split ratio was 80% for training data and the remaining 20% for testing and validation, following the best known practices for the training/testing ratio allocation. The training data were used to train the MLP, kNN, SVR and decision tree models, then find the optimal model parameters for each method. The remaining 20% of data were used to measure the final performance of the

implemented models. The error was measured based on RMSE, by comparing the actual solar irradiance readings with the forecasted values, as described in Eq. (10). After that, the forecast skill is obtained as shown in Eq. (13).

3. Datasets

The datasets used in this study were collected from KACARE, AERONET, and CAMS, covering the period of three years from January 14th, 2013 to December 31st, 2015 with a temporal resolution of one-hour. The data collection, cleaning and quality assurance techniques for each dataset are discussed below.

3.1. KACARE dataset

KACARE is a government agency responsible for the renewable energy legislation, analysis, measurements and research in Saudi Arabia. In 2013, KACARE started Renewable Recourse Monitoring and Mapping (RRMM) Solar Measurement Network. The goal of this RRMM Solar Measurement Network is to provide accurate ground-based measurements of solar radiation alongside the relevant weather parameters across the country. The total number of stations in the network is 53 (Zell et al., 2015).

The KACARE dataset used in this work was collected in Riyadh, Saudi Arabia, with exact site information as shown in the Table 3.

The used measurement instruments are listed in Table 4.

KACARE data are collected every minute during daytime, containing GHI, DNI, DHI and relative humidity readings. In this work, we have computed the one-hour average of these 1-min readings. So, for each hour HH:MM, we average all the minutes MM in that hour from MM = 00 to MM = 59, then use this averaged (GHI/DNI/DHI) value in the tested models as x_i^1, x_i^2 and x_i^3. In order to have more robust measurements, a secondary Pyranometer similar in make and model was installed at the same site to measure GHI, plus the rotating shadowband radiometer listed in Table 4. Data is collected from the secondary equipment in case of the failure of the primary equipment. The last column in Table 4 shows whether the equipment was used as a primary or a secondary for the measurements. For post processing data quality assurance NREL's Solar Energy Research Institute Quality Control (SERI-QC) procedures were followed (Maxwell et al., 1993). Data can be requested through KACARE Atlas website (KACARE; https://rratlas.kacare.gov.sa/).

3.2. AERONET dataset (AERONET; https://aeronet.gsfc.nasa.gov/)

The AERONET program is a remote sensing ground-based measurement network supported by NASA and many international institutions around the world. Their goal is to measure the AOD across different locations in the world and provide these measurements, alongside with microphysical properties, as an open access data.

AOD is a measure of the attenuation of radiation due to aerosols. AOD has no unit of measurements, i.e., unitless. The minimum AOD value is zero, which indicates that the atmosphere is clear. AOD value of 1 or more indicates a severe dust storm present in the scene. Depending on the type of aerosols to be estimated, AOD is measured at multiple wavelengths. In this work, the focus is to investigate the effect of dust, which is measured at 550 nm, using both ground-based and satellite-based measurements.

AOD equipment for the tested site is located at the same coordinates

Table 3
KACARE site information.

Latitude	24.90693° North
Longitude	46.39729° East
Elevation	764.0 Meters

Table 4
List of measurement Instruments.

Parameter	Equipment	Units	Uncertainty	Details
Relative Humidity	Relative Humidity Probe	% RH	± 3% to ± 7%	Primary
GHI	Pyranometer	W/m²	± 2.0%	Primary
GHI	Rotating Shadowband Radiometer	W/m²	± 5.0%	Secondary
DNI	Pyrheliometer	W/m²	± 2.0%	Primary
DNI	Rotating Shadowband Radiometer	W/m²	± 5.0%	Secondary
DHI	Pyranometer	W/m²	± 2.0%	Primary
DHI	Rotating Shadowband Radiometer	W/m²	± 5.0%	Secondary
AOD	CIMEL C-318 Sunphotometer	No unit	± 0.01 OD	Primary

shown in Table 3. This site has AOD readings at seven different wavelengths (i.e., 340, 380, 440, 500, 670, 870 and 1020 nm), as well as water vapor, solar zenith angle and the angstrom values. This study focuses on the wavelengths at 440 and 670, since they are used to extrapolate the AOD value at 550 nm, at which the dust concentration in the air is being measured. The extrapolation of AOD at 550 nm can be calculated as follows:

$$\tau_2 = \exp\left(\ln(\tau_1) - \alpha \ln\left(\frac{\lambda_2}{\lambda_1}\right)\right), \tag{14}$$

where τ_1 is the AOD at 440 nm; α is the Angstrom Exponent and it is a good indicator for the aerosol particle size in the air, $\alpha \leq 1$ indicates that the AOD particle distribution is mainly dominated by coarse mode particles, while $\alpha \geq 2$ represents an AOD distribution that is mainly dominated by a fine mode particles (Schuster et al., 2006), τ_2 is the desired AOD at 550 nm, at which the dust accumulation in the air is being measured. λ_1 and λ_2 are the wavelengths at 550 nm and 440 nm. Angstrom Exponent α can be found using the AOD readings at 440 nm and 670 as follows:

$$\alpha = \frac{\ln(\tau_3) - \ln(\tau_1)}{\ln(\lambda_3) - \ln(\lambda_1)}, \tag{15}$$

where τ_3 is the AOD value at 670 nm and λ_3 is the wavelength at 670 nm.

The dataset has multiple readings every hour without consistency in data reading intervals. However, in most of the days there is at least one reading every hour. If multiple readings are recorded for an hour HH:MM, all the readings through that hour (MM = 00 to MM = 59) are averaged, hence, we have one value per hour, this value is denoted as x_i^{10} as shown in Table 1. If one hour has a no readings, then the missing reading at this hour is substituted by implementing a linear interpolation. Fig. 6 shows histogram of how many distinct hours the AERONET AOD readings are measured each day for the tested site.

It can be seen that 92 days that have readings at 12 distinct hours. Clearly from the plot, some days have measurements only 1 h or 2 h. In this case linear interpolation will not provide realistic AOD values. Thus, in order to ensure the quality of input data, the dataset was selectively chosen to include only the days that have readings recorded for at least 6 distinct hours during that day. Data from AERONET are available at three quality levels: Level 1.0 is raw data collected from the measurement devices directly; Level 1.5 data are cloud screened; and Level 2.0 data are cloud screened and manually inspected (Smirnov et al., 2000). Level 1.5 data were used in this work due to the unavailability of Level 2.0 for the requested period of time. AOD data are measured using CIMEL C-318 sunphotometer (Myers et al., 2002).

3.3. CAMS dataset

CAMS is one of the Copernicus programs aimed to provide data on atmospheric composition at regional and global scale. It is managed by the European Commission (EU), in partnership with European Space Agency (ESA), the European Organization for the Exploitation of Meteorological Satellites (EUMETSAT) and the ECMWF.

The data contains many air quality parameters. It has AOD readings at five different wavelengths (i.e., 469, 550, 670, 865 and 1240 nm), Particulate Matter at different diameters (i.e., 10, 2.5, 1 μm), plus other weather parameters, such as temperature, wind speed, dew point temperature, cloud cover and albedo.

The CAMS system utilizes AOD data retrieved from both Polar Multi-Sensor Aerosol Product(PMA$_P$) provided by EUMETSAT, alongside with the AOD data retrieved from Moderate Resolution Imaging Spectroradiometer (MODIS) provided by NASA.

A grid size of 0.5° × 0.5° that contains the site indicated in Table 3 was used in this work. The temporal resolution of the CAMS data is based on 3 h forecasting step, starting from 00:00 UTC to 21:00 UTC for each day, so, for each day the available forecasts are for the hours 00:00, 03:00, 06:00, 09:00, 12:00, 15:00, 18:00 and 21:00, a total of 8 readings. In order to match the temporal resolution of the CAMS readings with other KACARE and AERONET datasets readings, a linear interpolation was performed on CAMS dataset, such that, a one reading was made available at each hour of the day. In this work, we implemented an hour-ahead forecasting model, hence, we used the forecasted CAMS AOD value for the next hour, which was already interpolated as discussed above. This CAMS AOD value is fed into the model as x_i^9, as shown in Table 1. All of CAMS data used in this work are available through ECMWF website (ECMWF; https://www.ecmwf.int/).

4. Data analysis

This section provides some insights and analysis about the dataset implemented in this work. Fig. 7 shows a windrose plot alongside with dust AOD values for the site under study in Riyadh, Saudi Arabia. The location is surrounded by two deserts, the Rub' Al-khali desert from the South and South East and Addahna desert from the North East. This makes the selected site a perfect choice for this work.

As can be clearly seen from the plot, the AOD values are highly dependent on the wind direction. The southern winds would have a higher chance of carrying dust particles, and in the second place the northern winds with a lower chance. This could be understood, knowing the fact that there is a large sand dessert laying at the southern side of the site, and another large desert laying at the northeastern side. Thus, any wind originating from these directions would have a higher probability of carrying sand particles, hence increasing the AOD value. Conversely, winds coming from the western side would have a lower probability of carrying dust particles. Therefore, dust intensity in the air is highly dependent on the wind direction. Accordingly, the solar irradiance is dependent on wind direction as well.

A scatter density plot to compare AERONET AOD at 550 nm (AOD_{550}) and CAMS AOD_{550} values is shown in Fig. 8. As can be clearly seen, CAMS AOD_{550} seems to overestimate the actual AERONET AOD_{550} readings. The correlation between the two datasets found to be 0.634. This moderate correlation coefficient means that CAMS AOD_{550} forecasts are uncertain. Accordingly, this would lead to a lower solar irradiance forecasts accuracy. Thus, a ground-based measurement for AOD_{550} would provide a correction factor for CAMS AOD_{550} forecasts for the next hour, hence, a more accurate solar irradiance forecasts.

Fig. 9 shows the AERONET AOD_{550} hourly readings histogram. The standard deviation is 0.3070 with the mean of 0.4413. Statistics of the remaining variables are shown in Table 5. The AOD_{550} covers the spectrum of clear sky to heavily dusty weather.

Fig. 10 shows the average monthly AOD_{550} for the test site, starting from 2013 to 2015, for both the AERONET and CAMS datasets. April
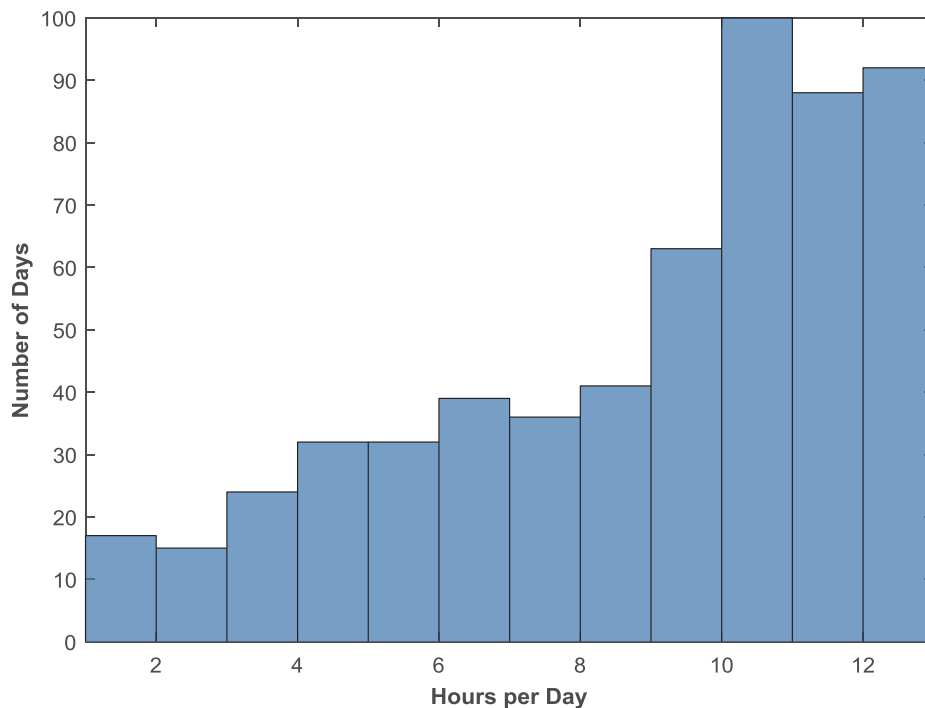
Fig. 6. Histogram of the number of hours the AOD was measured each day, based on the data provided by AERONET for KACARE sites.
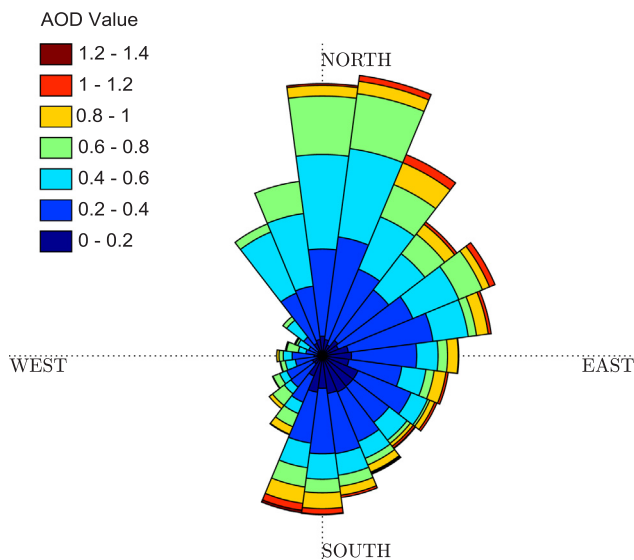

Fig. 7. Windrose plot versus AOD values.

then May have the highest AOD_{550} among all the other months in both datasets. Moreover, CAMS dataset appears to overestimate the AOD_{550} values most of the year except for the months starting from August to December. This over estimation in the AOD_{550} values obtained from CAMS dataset is expected as can be seen in Fig. 8.

In Fig. 11 the average behavior of (GHI/DNI/DHI) over the whole dataset is shown under different AOD values. As can be seen from the figure, DNI is the most sensitive radiation variable to AOD. DNI drops by roughly 60% when moving from clear atmosphere periods (AOD = 0) to periods with large aerosol presence (AOD = 1) caused by extreme dust events. On the other hand, DHI increases as AOD value increases. DHI increases by roughly 130% when moving from a clear sky condition to an extreme dust condition. Lastly, GHI is the least sensitive variable to AOD. That is mainly because GHI is composed of both DNI and DHI. Hence, any loss in the DNI component is partially

compensated by the increase in DHI component. As a result, the effect of AOD on GHI is limited.

5. Results and discussion

The forecasting model basic structure is shown in Fig. 3. The input variables for GHI/DNI/DHI forecasting models are listed in Tables 1 and 2. The construction of each forecasting method and the different subsets of the selected parameters are discussed in Section 2.

Table 6 shows the GHI results using the testing data under these different methods and feature selection schemes. Each row in Table 6 represents a set of selected features and each column represents the forecasting method used. For the first row in Table 6, features $x_i^1, x_i^4, \cdots, x_i^8$ are considered, they represent a set of features as described in Table 1, these features are considered the basic feature selection scheme in this work. As we move to the next row, when the CAMS AOD_{550} x_i^9 is added to the model, an improvement can be seen in all the models except for the kNN. Now, as we move to the last row, when we remove the CAMS AOD_{550} x_i^9 and add both the AERONET AOD_{550} x_i^{10} and the angstrom exponent x_i^{11}, improvement was observed in all tested models. When comparing the FSs for the MLP, kNN and SVR in the last row with the CAMS AOD_{550} model, an improvement of around 9%, 2% and 0.45% was observed, respectively. As can be seen from Table 6, when the new features are added, the RMSE and FS results for the MLP model kept on improving, while those for the SVR and kNN have no noticeable improvement. The smart persistence model for the GHI achieved an RMSE of 56.54 (W/m²), the values for this smart persistence model were computed as described in Eq. (12), and then the RMSE for this model was obtained as shown in Eq. (10). The GHI forecasting model implemented using the MLP has the best RMSE results on average, also it achieved the best RMSE result when the proposed features (i.e., x_i^{10} and x_i^{11}) were added. Moreover, MLP model has a FS improvement of around 16.6% when compared to the best performing model in the remaining models (i.e. kNN, SVR, decision tree).

On average the AOD_{550} effect on the GHI results across all tested methods is limited. To further analyze this effect, the MAPE for GHI forecasts was computed versus the AOD_{550} values under two solar zenith angles $\theta = 40°$ and $60°$. Fig. 12 shows the MAPE for the GHI model
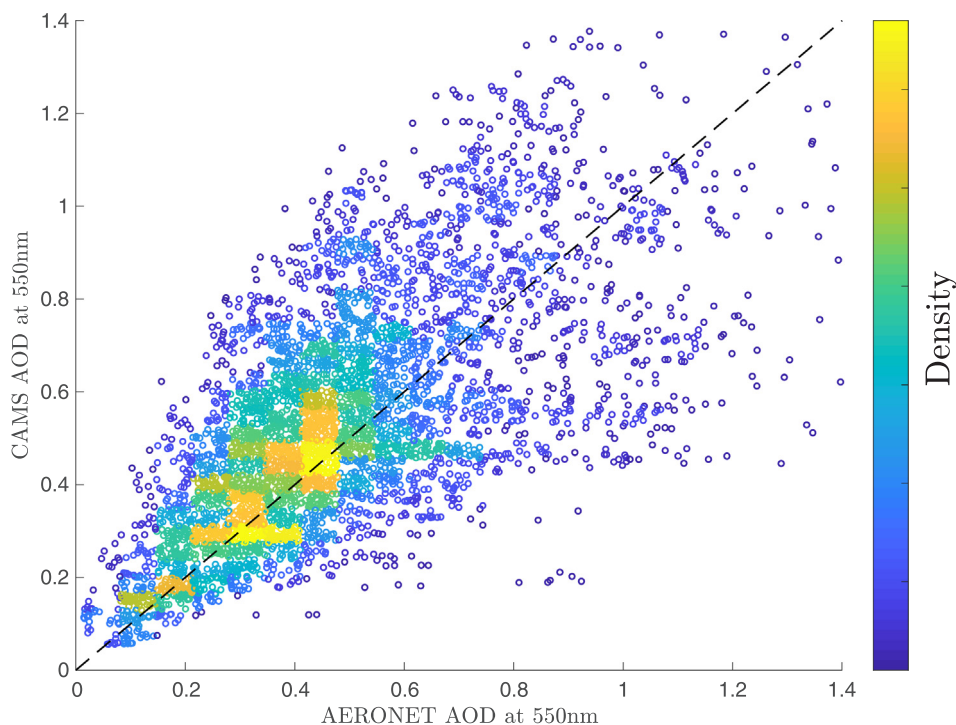
Fig. 8. AERONET AOD values at 550 nm vs. CAMS AOD values at 550 nm. The dashed line represents the ideal estimation case.

when tested under these two solar zenith angles, the MAPE for GHI has a slight increase as the AOD_{550} value increases, this is shown in Fig. 12 as the red and blue lines. Hence, the errors in the GHI forecasts increase as the AOD_{550} value increases. Moreover, the MAPE for GHI also increases as the solar zenith angle increases (i.e. the beginning and the end of the day). However, the MAPE tend to stay below 10% and around 5% on average. As can be seen from Fig. 12, the maximum MAPE for the GHI occurs at high AOD_{550} values. When $\theta = 60°$ the MAPE is around 10%, while for $\theta = 40°$ it's around 4%. Hence, AOD_{550} has some effect on GHI, however, this effect is limited, this can be

Table 5
Variables mean and standard deviation.

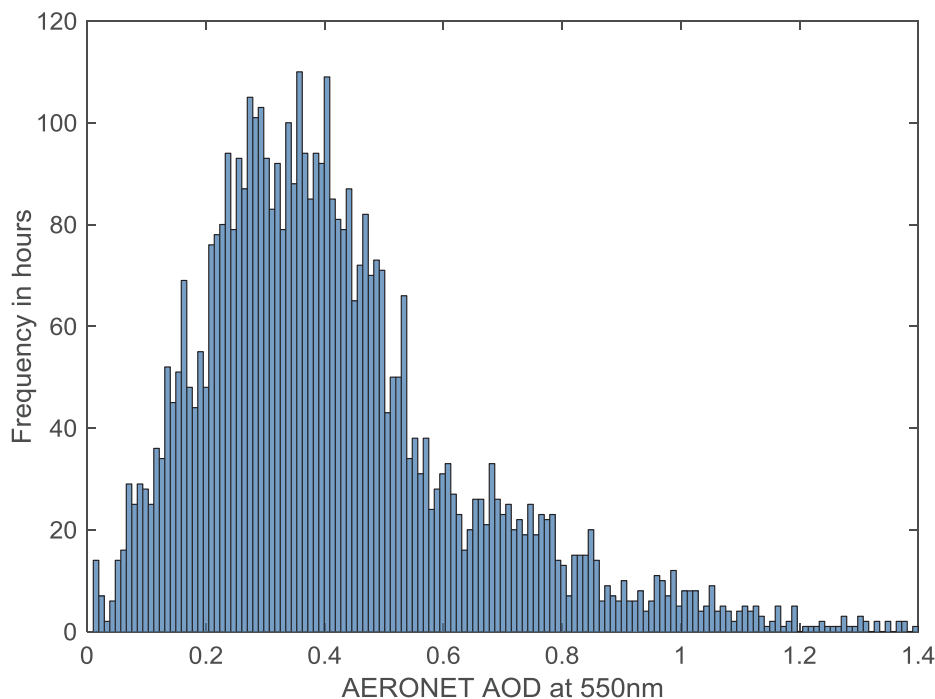|	Mean	Standard Deviation	Unit
GHI	620.34	272.96	W/m²
DNI	567.11	242.26	W/m²
DHI	221.63	112.82	W/m²
Wind Speed	4.212	1.75	m/s
AERONET AOD_{550}	0.4413	0.3070	–
CAMS AOD_{550}	0.5375	0.2569	–

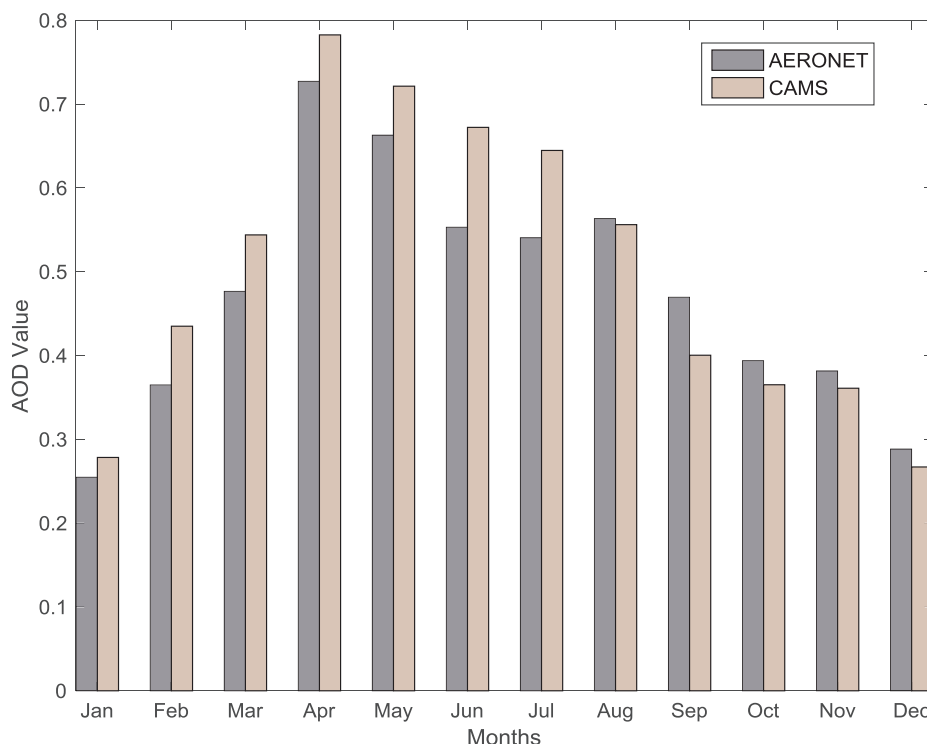**Fig. 9.** AERONET AOD at 550 nm histogram.

Fig. 10. AERONET and CAMS average AOD at 550 nm for each month of the year, using data from 2013 to 2015.

clearly seen in Table 6, as the AOD_{550} values were added to the models, only a limited improvement was observed in the RMSE values on average. The yellow lines and the right y-axis in the Fig. 12 show the GHI values under different AOD_{550} values, as for the MAPE, the GHI readings were also analyzed under two solar zenith angles $\theta = 40°$ and 60°. As can be seen from the yellow lines, the GHI values decrease as the AOD_{550} value increases. However, this decrease in the GHI value is

smooth and not steep as to be compared with DNI values later. The analysis using remaining solar zenith angles would lead to similar results. However, the results for $\theta = 40°$ and 60° are shown since the remaining zenith angles have some missing readings in the test data set under specific AOD values.

Overall, GHI results indicate that the MLP model outperformed all other methods as the new features were added. Hence, the MLP model
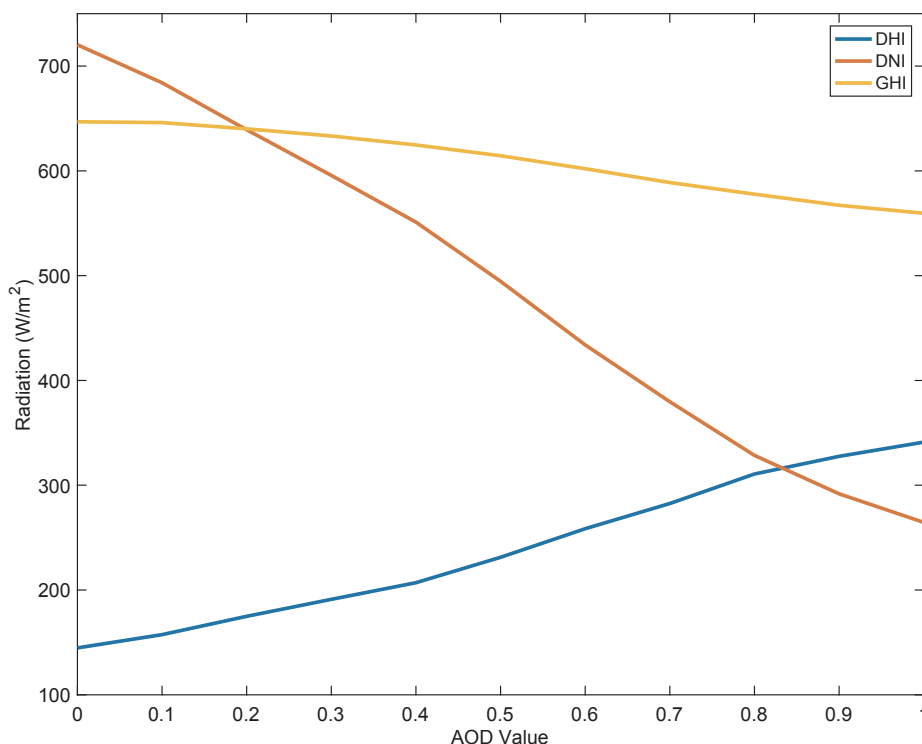

Fig. 11. (GHI/DNI/DHI) biases under different AOD values.

Table 6
RMSE results (W/m²) for GHI model and the forecast skill (FS).

Input variables	MLP		kNN		SVR		Decision tree	
	RMSE	FS %	RMSE	FS %	RMSE	FS %	RMSE	FS %
$x_i^1, x_i^4, \cdots, x_i^8$	38.24	32.35	38.15	32.52	57.97	-2.53	48.51	14.20
$x_i^1, x_i^4, \cdots, x_i^9$	37.78	33.16	43.23	23.52	56.37	0.28	45.78	19.08
$x_i^1, x_i^4, \cdots, x_i^8, x_i^{10}, x_i^{11}$	32.75	42.10	42.11	25.51	56.11	0.75	45.88	18.85

is able to understand the complexity and diversity of these features and keep minimizing the RMSE. On the other side, the kNN, SVR and decision tree methods seem to saturate around the same RMSE value as these new features were added. The RMSEs for training and testing datasets are shown in Fig. 13, for both kNN and SVR when they are tested under different feature selection schemes. It is apparent that these two models were overfitted when some features were added as can be seen in Fig. 13. The model parameters for kNN and SVR were optimally chosen based on the training set, the kNN model was tested under different number of neighbors k, the model's RMSE saturates around $k = 5$. Similarly, for the SVR, the model was tested under different C values, the optimum C value is found to be 1000. In Aybar-Ruiz et al. (2016), they were able to achieve a FS of 22% using their best subset of features including the GHI observed only at the last hour, in Grantham et al. (2016) they achieved 30.5% FS over the one-hour forecast horizon.

Table 7 shows DNI results under the same discussed models and feature selection schemes, the results presented were computed using the testing data discussed earlier. The parameters of the kNN and SVR models were optimized again for the DNI model following similar steps discussed earlier for the GHI model. The smart persistence model for the DNI achieved an RMSE of 102.40 (W/m²). As can be seen from Table 7, the accuracy of all the models kept on improving as more features were added.

In order to analyze this more, the MAPE for DNI is calculated under different AOD_{550} values. Fig. 14 shows the MAPE for DNI versus the AOD_{550} value for the model $x_i^2, x_i^4, \cdots, x_i^9$, where the ground observed AOD_{550} and angstrom exponent (i.e., x_i^{10} and x_i^{11}) were not added to the model yet. As before, MAPE for the DNI was measured at two solar

zenith angles $\theta = 40°$ and $60°$ shown in red and blue in Fig. 14. As can be seen from the plots, MAPE for the DNI increases noticeably as the AOD_{550} value increases. Hence, DNI value is very sensitive to AOD_{550} value under the clear sky conditions. The effect of AOD_{550} on DNI value is 3–4 times larger when compared to the GHI (Gueymard, 2012), this can be clearly seen when comparing the GHI and DNI errors in both Fig. 12 and Fig. 14 under the same θ. The maximum MAPE for the GHI when $\theta = 60°$ is about 10% while that for the DNI is around 45%. Moreover, the MAPE for DNI also increases as the solar zenith angle increases (i.e. the beginning and the end of the day). In Ruiz-Arias et al. (2016a, 2016b) they studied multiple AERONET locations around the world and classified the tested site (i.e. Riyadh, Saudi Arabia) as high turbidity site, moreover, they show that the AOD versus DNI relationship can be characterized by a linear estimation in low turbidity sites, however, for high turbidity sites the linear relationship is no longer applicable, hence, constructing a DNI forecasting model will be a harder problem in these sites. The yellow lines and the right y-axis in Fig. 14 show the DNI value under different AOD_{550} values, DNI values were computed under two solar zenith angles $\theta = 40°$ and $60°$. When the AOD_{550} value increases, a high drop in the DNI values is noticed for the same solar zenith angle θ.

Now, as the ground measured AERONET AOD_{550} x_i^{10} and the angstrom exponent x_i^{11} were added to the model, a good improvement in the RMSE and FS values was observed in all of the tested methods, with the MLP having the best RMSE and FS results among all of the other methods. As can be seen from Table 7, the ground measured AERONET AOD_{550} and the angstrom exponent (i.e., x_i^{10} and x_i^{11}) acted as a correction factor for the CAMS AOD_{550} (i.e., x_i^9) forecasts, hence, the FS for DNI model using MLP has improved by around 8.5% compared to the
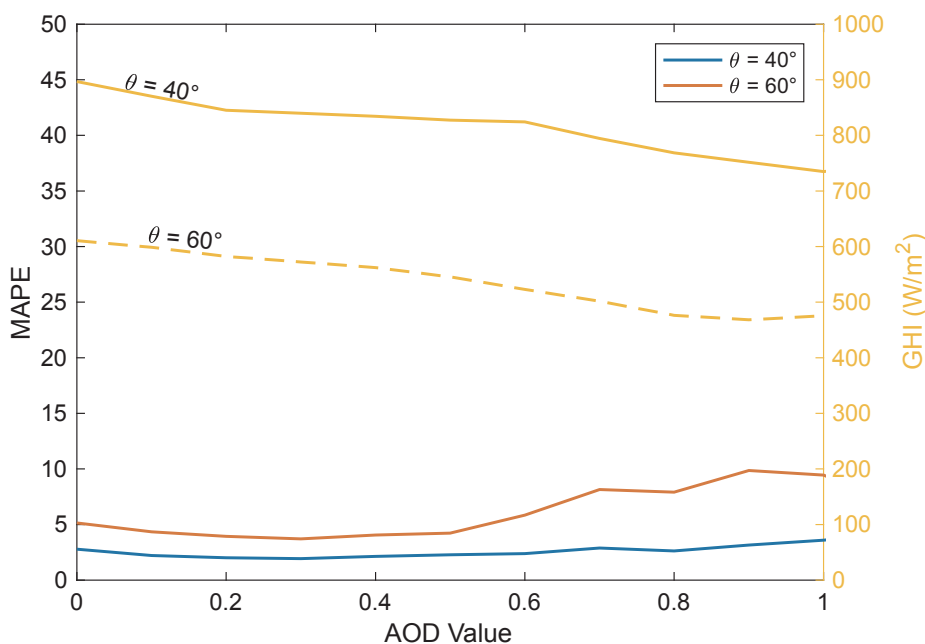

Fig. 12. Left y-axis shows MAPE for GHI vs AOD, right y-axis shows GHI value vs. AOD. The results were computed for different solar zenith angles $\theta = 40°$ and $60°$.
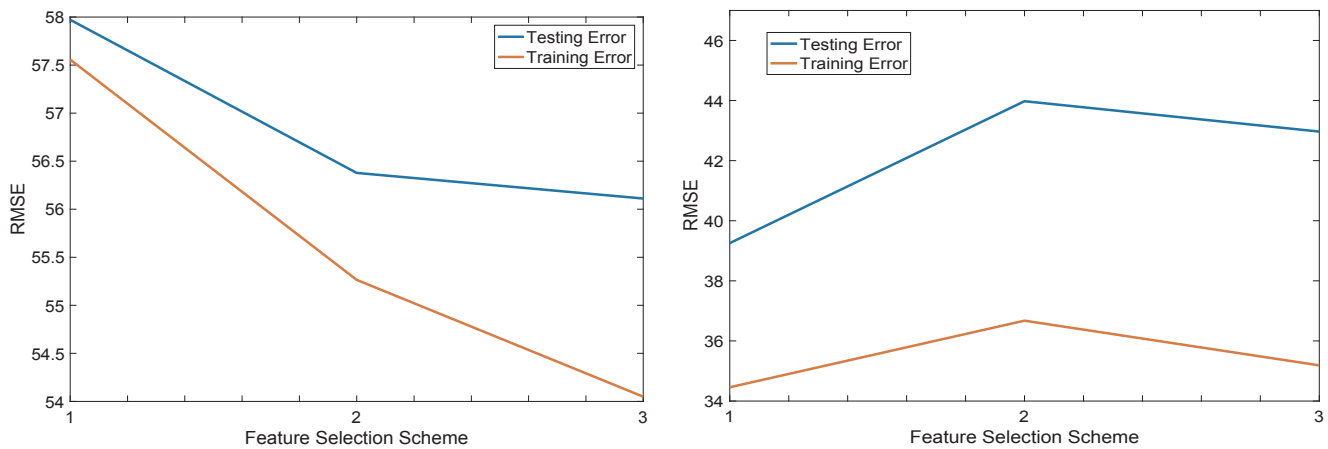
Fig. 13. the training and testing error for tested under two methods. (a) shows the RMSE values for the SVR model. (b) shows the RMSE for the kNN model.

Table 7
RMSE results (W/m^2) for DNI model and the forecast skill (FS).

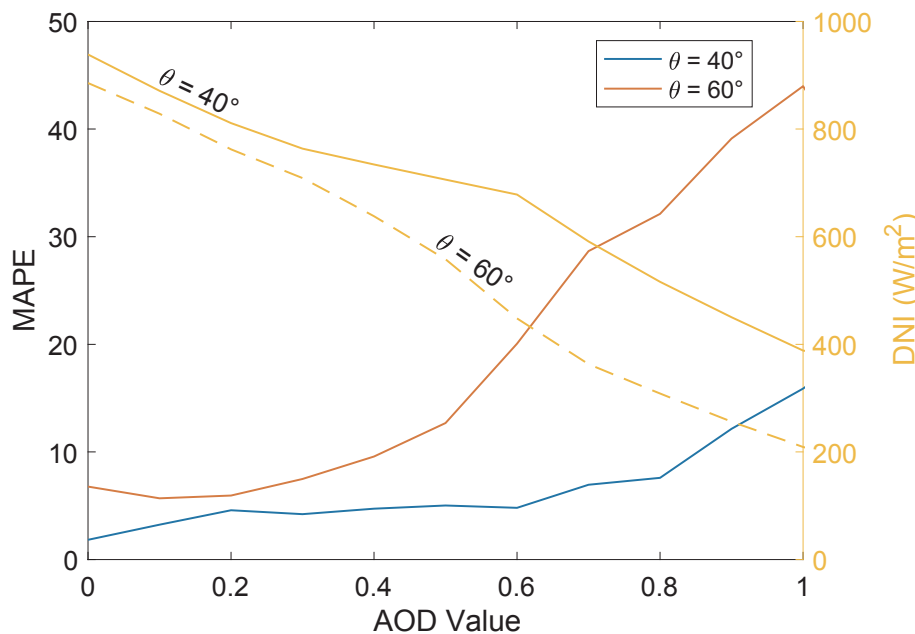| Input variables	MLP		kNN		SVR		Decision tree	
	RMSE	FS (%)	RMSE	FS (%)	RMSE	FS (%)	RMSE	FS (%)
$x_i^2, x_i^4, \cdots, x_i^8$	76.55	25.24	84.01	17.94	79.40	22.46	81.78	20.13
$x_i^2, x_i^4, \cdots, x_i^9$	72.06	29.62	83.64	18.31	78.52	23.31	81.47	20.43
$x_i^2, x_i^4, \cdots, x_i^8, x_i^{10}, x_i^{11}$	63.36	38.12	76.18	25.59	71.02	30.64	78.05	23.77

Fig. 14. Left y-axis shows MAPE for DNI vs AOD, right y-axis shows DNI value vs. AOD. The results were computed at different solar zenith angles $\theta = 40°$ and $60°$.

model where x_i^{10} and x_i^{11} were not added. The MLP model had an improvement of around 7.5% compared to the best performing model in the remaining models (i.e. kNN, SVR and decision tree). The kNN, SVR and decision tree models had all improved by around 7.28%, 7.3% and 3.34%, respectively, when the new features (i.e., x_i^{10} and x_i^{11}) were added. Overall, a noticeable improvement had been achieved among all the tested models when the new features (i.e., x_i^{10} and x_i^{11}) were added. This is to be expected, since the DNI is very sensitive to AOD_{550} values as shown in Fig. 14, hence, a more accurate AOD_{550} indicators would lead to better performing DNI forecasting model.

The performance of GHI and DNI using the MLP model was tested under extreme dust events that persisted for a number of days as these values are of special importance to grid operators. These parameters were analyzed for a period of three days starting from 6th to 8th of September 2013. This analysis was conducted using the best set of features as shown in the last row in Tables 6 and 7. The average AOD over these three days is 0.84. The AOD behavior during the daytime on these days is depicted in Fig. 15. The forecast skill for GHI when using MLP is 28.34%, whereas for the DNI it is 14.56%.

Table 8 shows the RMSE and FS for DHI model, measured using the testing dataset, under different methods and features selection schemes. The kNN and SVR models' parameters were optimized again for the DHI model following similar steps discussed earlier for the GHI model. The smart persistence model for the DHI achieved an RMSE of 41.59
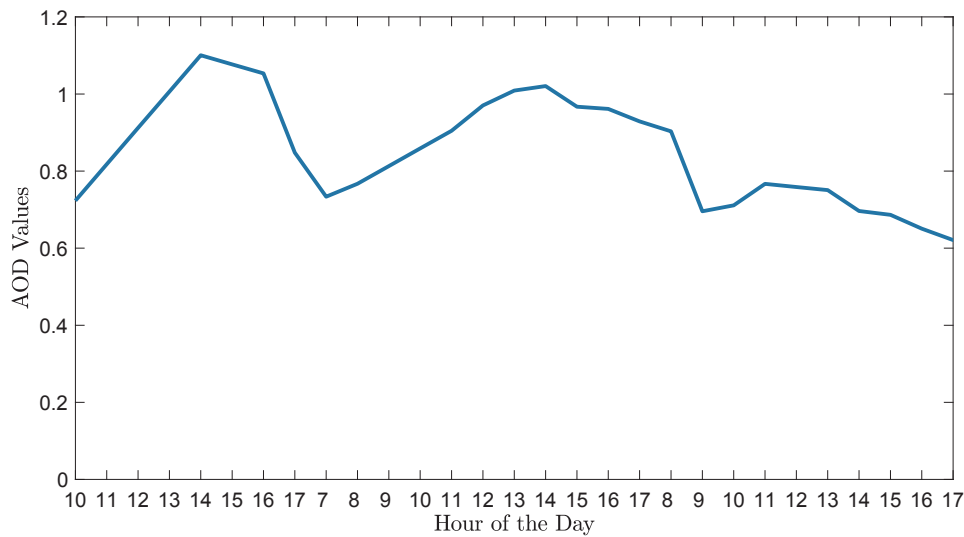
Fig. 15. Hourly AOD values during sand storm that persisted for three days, starting September 6th to 8th in 2013.

Table 8
RMSE results (W/m^2) for DHI model and the forecast skill (FS).

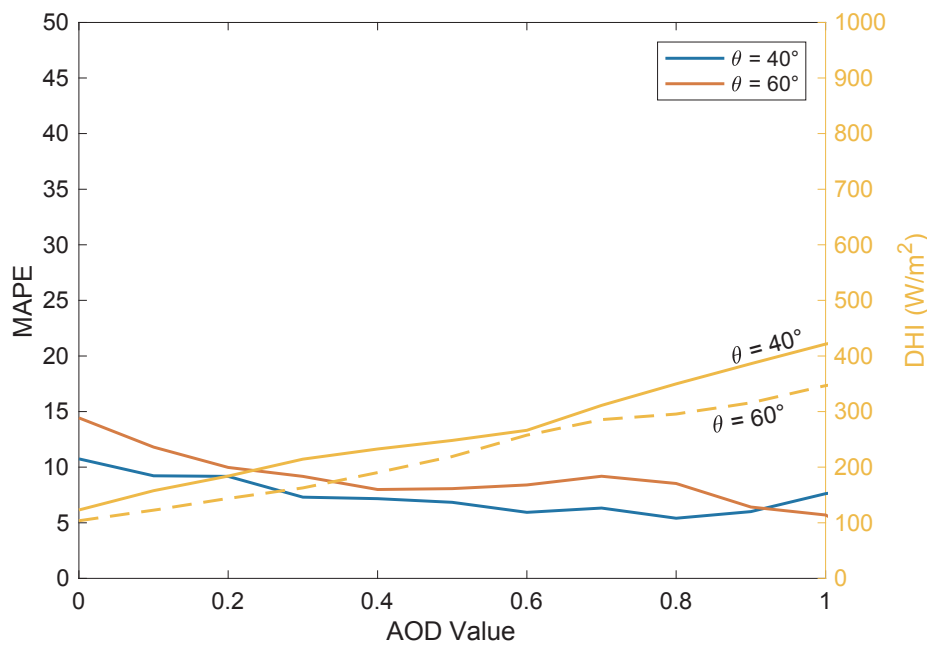| Input variables	MLP		kNN		SVR		Decision Tree	
	RMSE	FS (%)	RMSE	FS (%)	RMSE	FS (%)	RMSE	FS (%)
$x_i^3, x_i^4, \cdots, x_i^8$	31.00	25.45	35.66	14.25	37.89	8.9	36.36	12.56
$x_i^3, x_i^4, \cdots, x_i^9$	29.47	29.13	33.81	18.68	36.88	11.31	35.98	13.48
$x_i^3, x_i^4, \cdots, x_i^8, x_i^{10}, x_i^{11}$	23.90	42.52	30.88	25.73	35.02	15.78	30.79	25.96

Fig. 16. Left y-axis shows MAPE for DHI vs AOD, right y-axis shows DHI value vs. AOD. The results were computed at different solar zenith angels θ = 40° and 60°.

(W/m^2). On average, the MLP model outperformed all of the remaining methods under all feature selection schemes, the decision tree regression had the second best performance. As more features were added to these models, their RMSE and FS had improved for all of the tested methods. At first, improvement was observed when adding the CAMS AOD_{550} x_i^9 in all tested models. As the proposed features (i.e., x_i^{10} and x_i^{11}) were added, the overall accuracy has improved significantly across all models, and slightly for the SVR. For the MLP model, the FS has improved by around 13.4% when compared to the model that utilizes the CAMS AOD_{550}. Similarly, FS has improved by around 7% for the kNN, 4.5% for SVR and 12.5% for decision tree. As for the GHI and DNI models implemented earlier, the MLP model has shown a superior accuracy when compared to the other methods, moreover, the proposed features (i.e., x_i^{10} and x_i^{11}) increased the accuracy noticeably across all the tested methods.

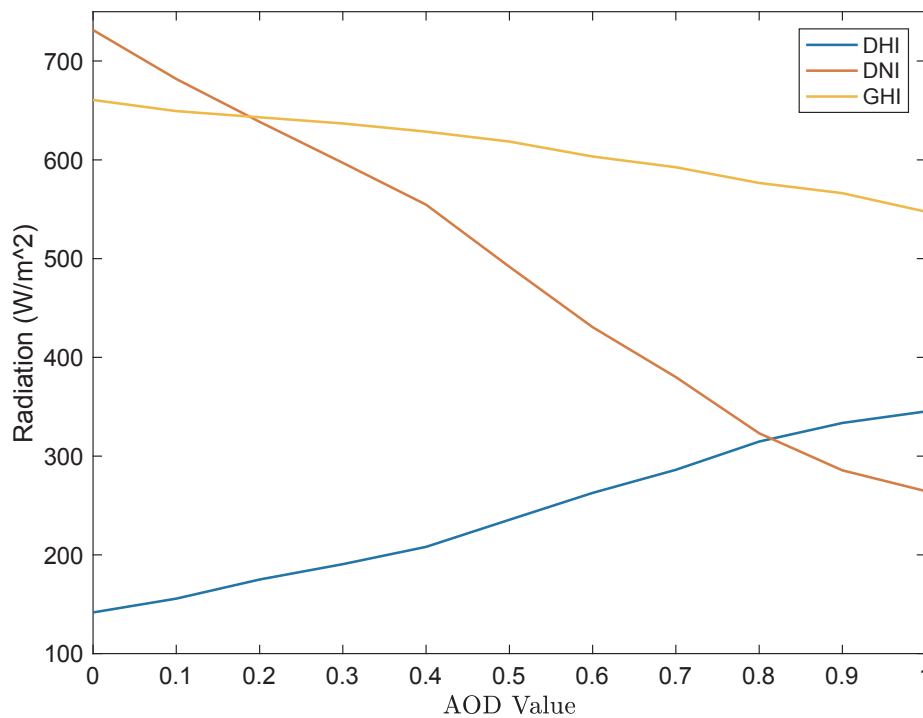Further analysis for the DHI performance versus the AOD_{550} value is

Fig. 17. MLP sensitivity under different AOD values for GHI, DNI and DHI.

Table 9
RMSE results (W/m²) for (GHI/DNI/DHI) models under different training and testing splitting ratios averaged using all methods.

Split Ratio (training/testing)	Radiation Variables		
	GHI	DNI	DHI
85/15	47.44	71.68	29.93
80/20	43.75	70.60	30.14
75/25	44.60	71.62	31.14

Table 10
RMSE results (W/m²) for all methods under low and high AOD values.

Radiation Variables	AOD Range	Method			
		MLP	kNN	SVR	Decision Tree
GHI	AOD ≤ 0.5	25.28	31.90	52.42	41.72
	AOD > 0.5	43.43	56.47	66.46	59.52
DNI	AOD ≤ 0.5	51.43	65.86	67.49	74.13
	AOD > 0.5	67.27	90.46	73.77	81.19
DHI	AOD ≤ 0.5	21.25	26.49	35.37	25.72
	AOD > 0.5	27.97	36.92	35.99	39.37

shown in Fig. 16. The MAPE for DHI decreases as the AOD_{550} value increases. The MAPE is relatively small when compared to the MAPE for DNI model under the same solar zenith angle. For example, when $\theta = 60°$, the maximum MAPE for the DHI model is about 15%, while for the DNI model it's is about 45%. As with the previous models, the MAPE for DHI increases as the solar zenith angle increases (i.e. at the beginning and the end of the day). The DHI readings were also compared with the AOD_{550} values in Fig. 16 as shown in yellow lines and the right y-axis. As can be clearly seen, the DHI readings increase as the AOD_{550} value increases. This is mainly because of the radiation scattering caused by the AOD_{550} particles in the air. Overall, a significant improvement has be achieved when the new features were added to the model, that's due to the fact that DHI is moderately sensitive to AOD_{550} as shown in Fig. 16. Hence, feeding the tested models with the new set

of features (i.e., x_i^{10} and x_i^{11}), would lead to an improved accuracy for the DHI forecasting model across all the implemented methods. Fig. 17 shows the MLP model sensitivity for (GHI/DNI/DHI) under different AOD values. As can be seen from the figure and as discussed earlier in Fig. 11, the DNI is the most sensitive radiation variable to dust; DHI is less sensitive to dust when compared to DNI; and GHI is the least sensitive to dust.

All implemented models were tested under different ratios of training/testing datasets. Table 9 shows the resulted RMSE values averaged over all implemented models for all radiation variables (GHI/DNI/DHI) when tested under the best feature selection scheme. Overall, the error variation under different allocations of training/testing datasets is limited.

The performance of all methods has been tested under high and low AOD. Low values are when AOD ≤ 0.5, whereas high values are when AOD > 0.5. Table 10 shows the performance of all tested models under the high and low AOD values for all radiation variables (GHI/DNI/DHI). As shown, MLP has the best performance among all methods under all radiation variables, for both the high and low AOD value cases. As can be seen from results, the accuracy of all methods decreases when AOD values are high. Fig. 18 shows the MAPE performance for (GHI/DNI/DHI) for each month of the year. MAPE has a slight increase for high AOD months for both GHI and DNI, whereas for DHI the MAPE decreases during these months. The models' performance has been analyzed for periods with above average variability values. The average and standard deviation for these inputs are shown in Table 5. Only periods with at least 10% standard deviation values above the average were tested. The variables that were considered are the variables that change inconsistently over the day, these variables are the AOD, wind speed, wind direction. Table 11 shows the performance of the different radiation variables across all the models when tested under high variability periods. As can be seen from Table 11, the MLP and Decision Tree models are the most robust models during high variability periods.

6. Conclusion

An hour ahead solar forecasting model based on new features scheme for GHI/DNI/DHI was introduced in this work. The new
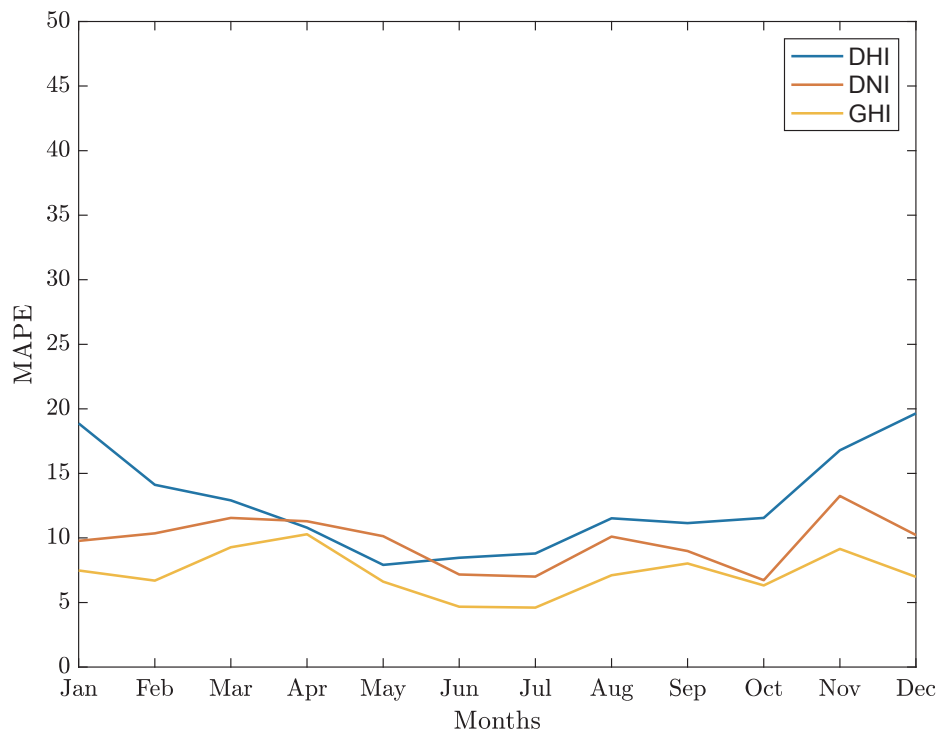
Fig. 18. MAPE Averaged over all methods for each month of the year.

Table 11
RMSE results (W/m²) for all methods during high variability periods.

Method	Radiation variables		
	GHI	DNI	DHI
MLP	25.76	39.72	20.74
kNN	39.29	48.24	23.92
SVR	45.07	53.83	27.88
Decision Tree	20.98	37.78	18.10

introduced features are fed into an hour-ahead solar forecasting models, these models are all data driven models. The introduced features are, the ground observed AOD at 550 nm observed at the last hour and the angstrom exponent, alongside with other meteorological variables as shown in Table 1. The solar forecasting model was constructed using real data gathered from three different resources, KACARE, AERONET and CAMS over three years period and one-hour temporal resolution. The MLP solar forecasting model was tested and compared alongside with SVR, kNN and decision tree regression. Results indicated that the MLP model outperformed all of the other forecasting models with and without the addition of the new proposed features. However, the addition of the proposed features improved all of the GH/DNI/DHI forecasting models significantly. The best performing forecasting model was the MLP with RMSE of 32.75 (W/m²) and FS of 42.10% for the GHI forecasting model, RMSE of 63.36 (W/m²) and FS of 38.12% for the DNI forecasting model, RMSE of 23.90 (W/m²) and FS of 42.52 for the DHI forecasting model. On average, a high improvement was observed when the new set of features were added to the DNI model, this is related to the fact that DNI very sensitive to AOD values as shown in Fig. 14. Moreover, the DNI is 3–4 times more sensitive to AOD values when compared to the GHI under clear sky conditions (Gueymard, 2012). In addition, the tested site is considered a high turbidity site (i.e. high AOD values all over the year) (Ruiz-Arias et al., 2016a, 2016b) compared to other sites in the worlds, hence, the utilization of the new set of features in the forecasting models would assist the models' overall performance and increase the accuracy significantly as presented in

Tables 6–8.

Possible future directions to improve the work would revolve mainly around the extension of the time horizon into a few hours ahead, then study the effect of the new proposed features under this extended time horizon. Moreover, the time horizon could be extended into a day ahead, since AOD caused by the sand storms would usually stay in the air for a couple of days, hence, the observation of the AOD at the previous day would be beneficial for the next day irradiance forecast.

In summary, the proposed model can benefit grid operators, especially in areas where the dust storms have frequent presence and the AOD is high (> 0.4) all over the year.

References

Abdel Gelil, Ibrahim, Howarth, Nicholas, Lanza, Alessandro, 2017. Growth, Investment and the Low-Carbon Transition: A View from Saudi Arabia. KAPSARC.

Alzahrani, A., Shamsi, P., Dagli, C., Ferdowsi, M., 2017. Solar irradiance forecasting using deep neural networks. Proc. Comput. Sci. 114, 304–313. http://dx.doi.org/10.1016/J.PROCS.2017.09.045.

Alqatari, S., Alfaris, A., Weck, O.L. De, 2015. Cost and performance comparative model of dust mitigation technologies for solar PV in Saudi Arabia. Int. Sci. J. Environ. Sci. 4.

Antonanzas, J., Osorio, N., Escobar, R., Urraca, R., Martinez-de-Pison, F.J., Antonanzas-Torres, F., 2016. Review of photovoltaic power forecasting. Sol. Energy. http://dx.doi.org/10.1016/j.solener.2016.06.069.

Asif, M., 2016. Urban scale application of solar PV to improve sustainability in the building and the energy sectors of KSA. Sustainability 8. http://dx.doi.org/10.3390/su8111127.

Aybar-Ruiz, A., Jiménez-Fernández, S., Cornejo-Bueno, L., Casanova-Mateo, C., Sanz-Justo, J., Salvador-González, P., Salcedo-Sanz, S., 2016. A novel grouping genetic algorithm-extreme learning machine approach for global solar radiation prediction from numerical weather models inputs. Sol. Energy 132, 129–142. http://dx.doi.org/10.1016/j.solener.2016.03.015.

Azadeh, A., Maghsoudi, A., Sohrabkhani, S., 2009. An integrated artificial neural

networks approach for predicting global radiation. Energy Convers. Manag. 50, 1497–1505. http://dx.doi.org/10.1016/j.enconman.2009.02.019.

Belaid, S., Mellit, A., 2016. Prediction of daily and mean monthly global solar radiation using support vector machine in an arid climate. Energy Convers. Manag. 118, 105–118. http://dx.doi.org/10.1016/j.enconman.2016.03.082.

Cesnulyte, V., Lindfors, A.V., Pitkänen, M.R.A., Lehtinen, K.E.J., Morcrette, J.J., Arola, A., 2014. Comparing ECMWF AOD with AERONET observations at visible and UV wavelengths. Atmos. Chem. Phys. 14, 593–608. http://dx.doi.org/10.5194/acp-14-593-2014.

Chu, Y., Coimbra, C.F.M., 2017. Short-term probabilistic forecasts for Direct Normal Irradiance. Renew. Energy 101, 526–536. http://dx.doi.org/10.1016/j.renene.2016.09.012.

Coimbra, C.F.M., Kleissl, J., Marquez, R., 2013. Overview of solar-forecasting methods and a metric for accuracy evaluation. Sol. Energy Forecast. Resource Assess. 171–194. http://dx.doi.org/10.1016/B978-0-12-397177-7.00008-5.

Eissa, Y., Marpu, P.R., Gherboudj, I., Ghedira, H., Ouarda, T.B.M.J., Chiesa, M., 2013. Artificial neural network based model for retrieval of the direct normal, diffuse horizontal and global horizontal irradiances using SEVIRI images. Sol. Energy 89, 1–16. http://dx.doi.org/10.1016/j.solener.2012.12.008.

Gensler, A., Henze, J., Sick, B., Raabe, N., 2017. Deep Learning for solar power forecasting - An approach using AutoEncoder and LSTM Neural Networks. In: 2016 IEEE International Conference on Systems, Man, and Cybernetics, SMC 2016 - Conference Proceedings, pp. 2858–2865. https://doi.org/10.1109/SMC.2016.7844673.

Ghayekhloo, M., Ghofrani, M., Menhaj, M.B., Azimi, R., 2015. A novel clustering approach for short-term solar radiation forecasting. Sol. Energy 122, 1371–1383. http://dx.doi.org/10.1016/j.solener.2015.10.053.

Grantham, A., Gel, Y.R., Boland, J., 2016. Nonparametric short-term probabilistic forecasting for solar radiation. Sol. Energy 133, 465–475. http://dx.doi.org/10.1016/j.solener.2016.04.011.

Gueymard, C.A., 2012. Temporal variability in direct and global irradiance at various time scales as affected by aerosols. Sol. Energy 86, 3544–3553. http://dx.doi.org/10.1016/j.solener.2012.01.013.

Gulin, M., Pavlovic, T., Vašak, M., 2017. A one-day-ahead photovoltaic array power production prediction with combined static and dynamic on-line correction. Sol. Energy 142, 49–60. http://dx.doi.org/10.1016/j.solener.2016.12.008.

Gutierrez-Corea, F.V., Manso-Callejo, M.A., Moreno-Regidor, M.P., Manrique-Sancho, M.T., 2016. Forecasting short-term solar irradiance based on artificial neural networks and data from neighboring meteorological stations. Sol. Energy 134, 119–131. http://dx.doi.org/10.1016/j.solener.2016.04.020.

Hassan, G., Yilbas, B.S., Abdul Samad, M., Ali, H., Al-Sulaiman, F.A., Al-Aqeeli, N., 2017. Analysis of environmental dust and mud adhesion on aluminum surface in relation to solar energy harvesting. Sol. Energy 153, 590–599. http://dx.doi.org/10.1016/j.solener.2017.06.015.

Hu, Q., Zhang, R., Zhou, Y., 2016. Transfer learning for short-term wind speed prediction with deep neural networks. Renew. Energy 85, 83–95. http://dx.doi.org/10.1016/j.renene.2015.06.034.

Ibrahim, I.A., Khatib, T., 2017. A novel hybrid model for hourly global solar radiation prediction using random forests technique and firefly algorithm. Energy Convers. Manag. 138, 413–425. http://dx.doi.org/10.1016/j.enconman.2017.02.006.

IEA, 2017. Tracking Clean Energy Progress 2017.

Ineichen, P., Perez, R., 2002. A new airmass independent formulation for the linke turbidity coefficient. Sol. Energy 73, 151–157. http://dx.doi.org/10.1016/S0038-092X(02)00045-2.

Jiang, Y., Lu, L., Lu, H., 2016. A novel model to estimate the cleaning frequency for dirty solar photovoltaic (PV) modules in desert environment. Sol. Energy 140, 236–240. http://dx.doi.org/10.1016/j.solener.2016.11.016.

Kingma, D.P., Ba, J.L., 2015. Adam: a Method for Stochastic Optimization. Int. Conf. Learn. Represent, pp. 1–15. http://doi.acm.org.ezproxy.lib.ucf.edu/10.1145/1830483.1830503.

Li, L.-L., Cheng, P., Lin, H.-C., Dong, H., 2017. Short-term output power forecasting of photovoltaic systems based on the deep belief net. Adv. Mech. Eng. 9http://dx.doi.org/10.1177/1687814017715983. 168781401771598.

Jamaly, M., Kleissl, J., 2017. Spatiotemporal interpolation and forecast of irradiance data using Kriging spatiotemporal interpolation and forecast of irradiance data. Sol. Energy 158, 407–423. http://dx.doi.org/10.1016/j.solener.2017.09.057.

Maxwell, E., Wilcox, S., Rymes, M., 1993. Users Manual for SERI QC Software, Assessing the Quality of Solar Radiation Data. Solar Energy Research Institute, Golden, CO.

Mocanu, E., Nguyen, P.H., Gibescu, M., Kling, W.L., 2016. Deep learning for estimating building energy consumption. Sustain. Energy, Grids Networks 6, 91–99. http://dx.doi.org/10.1016/j.segan.2016.02.005.

Myers, D., Wilcox, S., Marion, W., Al-Abbadi, N., 2002. Final Report for Annex II– Assessment of Solar Radiation Resources In Saudi Arabia, 1998–2000.

Nabavi, S.O., Haimberger, L., Samimi, C., 2016. Climatology of dust distribution over West Asia from homogenized remote sensing data. Aeolian Res. 21, 93–107. http://dx.doi.org/10.1016/j.aeolia.2016.04.002.

Notaro, M., Alkolibi, F., Fadda, E., Bakhrjy, F., 2013. Trajectory analysis of Saudi Arabian dust storms. J. Geophys. Res. Atmos. 118, 6028–6043. http://dx.doi.org/10.1002/jgrd.50346.

Olatomiwa, L., Mekhilef, S., Shamshirband, S., Mohammadi, K., Petković, D., Sudheer, C., 2015. A support vector machine-firefly algorithm-based model for global solar radiation prediction. Sol. Energy 115, 632–644. http://dx.doi.org/10.1016/j.solener.2015.03.015.

Pedro, H.T.C., Coimbra, C.F.M., 2015a. Nearest-neighbor methodology for prediction of intra-hour global horizontal and direct normal irradiances. Renew. Energy 80, 770–782. http://dx.doi.org/10.1016/j.renene.2015.02.061.

Pedro, H.T.C., Coimbra, C.F.M., 2015b. Short-term irradiance forecastability for various solar micro-climates. Sol. Energy 122, 587–602. http://dx.doi.org/10.1016/j.solener.2015.09.031.

Perez, R., Ineichen, P., Moore, K., Kmiecik, M., Chain, C., George, R., Vignola, F., 2002. A new operational model for satellite-derived irradiances: description and validation. Sol. Energy 73, 307–317. http://dx.doi.org/10.1016/S0038-092X(02)00122-6.

Pierro, M., Bucci, F., De Felice, M., Maggioni, E., Moser, D., Perotto, A., Spada, F., Cornaro, C., 2016. Multi-model ensemble for day ahead prediction of photovoltaic power generation. Sol. Energy 134, 132–146. http://dx.doi.org/10.1016/j.solener.2016.04.040.

Qiu, X., Zhang, L., Ren, Y., Suganthan, P., Amaratunga, G., 2014. Ensemble deep learning for regression and time series forecasting. In: IEEE SSCI 2014 - 2014 IEEE Symposium Series on Computational Intelligence - CIEL 2014: 2014 IEEE Symposium on Computational Intelligence in Ensemble Learning, Proceedings. https://doi.org/10.1109/CIEL.2014.7015739.

Rana, M., Koprinska, I., Agelidis, V.G., 2016. Univariate and multivariate methods for very short-term solar photovoltaic power forecasting. Energy Convers. Manag. 121, 380–390. http://dx.doi.org/10.1016/j.enconman.2016.05.025.

Ruiz-Arias, J.A., Gueymard, C.A., Santos-Alamillos, F.J., Pozo-Vázquez, D., 2016a. Worldwide impact of aerosol's time scale on the predicted long-term concentrating solar power potential. Sci. Rep. 6, 30546. http://dx.doi.org/10.1038/srep30546.

Ruiz-Arias, J.A., Gueymard, C.A., Santos-Alamillos, F.J., Quesada-Ruiz, S., Pozo-Vázquez, D., 2016b. Bias induced by the AOD representation time scale in long-term solar radiation calculations. Part 2: Impact on long-term solar irradiance predictions. Sol. Energy 135, 625–632. http://dx.doi.org/10.1016/j.solener.2016.06.017.

Sarver, T., Al-Qaraghuli, A., Kazmerski, L.L., 2013. A comprehensive review of the impact of dust on the use of solar energy: history, investigations, results, literature, and mitigation approaches. Renew. Sustain. Energy Rev. http://dx.doi.org/10.1016/j.rser.2012.12.065.

Schuster, G.L., Dubovik, O., Holben, B.N., 2006. Angstrom exponent and bimodal aerosol size distributions. J. Geophys. Res. Atmos. 111. http://dx.doi.org/10.1029/2005JD006328.

Ryu, Seunghyoung, Noh, Jaekoo, Kim, Hongseok, 2016. Deep neural network based demand side short term load forecasting. In: 2016 IEEE International Conference on Smart Grid Communications (SmartGridComm), pp. 308–313. https://doi.org/10.1109/SmartGridComm.2016.7778779.

Shi, X., Chen, Z., Wang, H., Yeung, D.-Y., Wong, W., Woo, W., 2015. Convolutional LSTM Network: A Machine Learning Approach for Precipitation Nowcasting.

Smirnov, A., Holben, B.N., Eck, T.F., Dubovik, O., Slutsker, I., 2000. Cloud-screening and quality control algorithms for the AERONET database. Rem. Sens. Environ. 73, 337–349. http://dx.doi.org/10.1016/S0034-4257(00)00109-7.

Sulaiman, S.A., Singh, A.K., Mokhtar, M.M.M., Bou-Rabee, M.A., 2014. Influence of dirt accumulation on performance of PV panels. Energy Proc. 50–56. http://dx.doi.org/10.1016/j.egypro.2014.06.006.

Wang, H., Yi, H., Peng, J., Wang, G., Liu, Y., Jiang, H., Liu, W., 2017. Deterministic and probabilistic forecasting of photovoltaic power based on deep convolutional neural network. Energy Convers. Manag. 153, 409–422. http://dx.doi.org/10.1016/j.enconman.2017.10.008.

Yang, D., Ye, Z., Lim, L.H.I., Dong, Z., 2015. Very short term irradiance forecasting using the lasso. Sol. Energy 114, 314–326. http://dx.doi.org/10.1016/j.solener.2015.01.016.

Zell, E., Gasim, S., Wilcox, S., Katamoura, S., Stoffel, T., Shibli, H., Engel-Cox, J., Al Subie, M., 2015. Assessment of solar radiation resources in Saudi Arabia. Sol. Energy 119, 422–438. http://dx.doi.org/10.1016/j.solener.2015.06.031.